Talanta 265 (2023) 124842

Contents lists available at ScienceDirect

Talanta

journal homepage: www.elsevier.com/locate/talanta

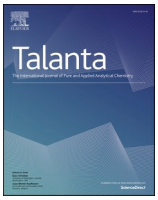

# 2D-$ReS_2$ & diamond nanoparticles-based sensor for the simultaneous determination of sunset yellow and tartrazine in a multiple-pulse amperometry FIA system

Ricardo Garsed [a], Luis Vázquez [b], Elena Casero [a], M Dolores Petit-Domínguez [a], Carmen Quintana [a], María del Pozo [a,*]

[a] Departamento de Química Analítica y Análisis Instrumental, Facultad de Ciencias, Universidad Autónoma de Madrid. Campus de Excelencia de La Universidad Autónoma de Madrid, C/ Francisco Tomás y Valiente, N°7, 28049, Madrid, Spain
[b] Instituto de Ciencia de Materiales de Madrid (ICMM), CSIC, Campus de Excelencia de La Universidad Autónoma de Madrid, C/ Sor Juana Inés de La Cruz N°3, 28049, Madrid, Spain

ARTICLE INFO

Handling Editor:J.-M. Kauffmann

*Keywords:*
Flow injection analysis with multiple-pulse amperometry detection
Transition metal dichalcogenides
Colourants
Diamond nanoparticles
Rhenium disulfide
Jelly sample

ABSTRACT

We present a flow injection system with a multiple pulse amperometric detection (FIA-MPA)-based methodology for the simultaneous analysis of sunset yellow and tartrazine. As transducer, we have developed a novel electrochemical sensor based on the synergistic effect of $ReS_2$ nanosheets and diamond nanoparticles (DNPs). Among several transition dichalcogenides for the sensor development, we have selected $ReS_2$ nanosheets since it yields a better response towards both colourants. Scanning probe microscopy characterization shows that the surface sensor is composed by scattered and stacked $ReS_2$ flakes and large aggregates of DNPs. With this system, the gap between the oxidation potential values of sunset yellow and tartrazine is wide enough to allow the simultaneous determination of both dyes. Under the optimum potential pulse conditions (0.8 and 1.2 V) during 250 ms, a flow rate of 3 mL/min and a volume injection of 250 μL, detection limits of $3.51 \times 10^{-7}$ M and $2.39 \times 10^{-7}$ M for sunset yellow and tartrazine, respectively, were obtained. This method exhibits good accuracy and precision with Er minor than 13% and RSD lower than 8% with a sampling frequency of 66 samples per hour. Pineapple jelly samples were analyzed by the standard addition method, obtaining 53.7 mg/kg and 29.0 mg/kg of sunset yellow and tartrazine, respectively. From the analysis of fortified samples, recoveries of 94% and 105% were obtained.

## 1. Introduction

Since its discovery, graphene has been widely explored for different applications including the development of electrochemical sensors. In recent years, research in this field has focused on exploring new 2D materials. In particular, the use of transition metal dichalcogenides (TMDs) has increased due to their attractive properties [1,2].

TMDs exhibit a $MX_2$ sandwich structure formed by a transition metal atom located between two layers of chalcogen atoms. These $MX_2$ layers are weakly bound by van der Waals forces [3]. The synthesis procedures to obtain 2D-TMDs are classified as top-down and bottom-up methods. Briefly, the most employed bottom-up methods are chemical vapour deposition (CVD) and liquid phase exfoliation [4]. The main advantage of CVD is that allows to obtain TMDs monolayers on a substrate while solution chemical processes make it possible to obtain powders of different shapes. Top-down methods, such as solvent liquid exfoliation assisted by ultrasounds, can be employed thanks to the weak interaction between the layers. This method allows to obtain TMDs layers in large quantities and, for this reason, this is a widely used procedure for 2D-TMDs synthesis [5].

Most of the works related to the use of TMDs nanosheets for different applications involve the use of $MoS_2$ or $WS_2$ [6–11]. In applications related to electrochemical sensor development, these materials are usually combined with other nanomaterials of different dimension [6]. In previous works, we have demonstrated the synergistic effect obtained by the combination of $MoS_2$ or $WS_2$ with diamond nanoparticles (DNPs) for the electrode modification [7–9]. The modification of the electrode surface with $WS_2$ nanosheets and DNPs, employed for the determination of two food dyes, not only resulted in an increase in the peak current of both analytes, but also in the separation of the overlapped dye signals

* Corresponding author.
*E-mail address:* maria.delpozo@uam.es (M. del Pozo).

https://doi.org/10.1016/j.talanta.2023.124842
Received 17 February 2023; Received in revised form 6 June 2023; Accepted 19 June 2023
Available online 20 June 2023

obtained with the bare electrode, thus allowing their simultaneous quantification [9]. The layer structure of the TMD increases the electroactive area, while the DNPs contribute with their catalytic properties. Recently, other transition metal disulfides as $ReS_2$ or $TiS_2$ have been synthesized, but their analytical applications are still scarce, being mainly focused on the determination of gas molecules like $O_2$ or $H_2S$ [12–14]. In particular, for $ReS_2$, some examples have been reported using optical methodologies but the electrochemical sensing field remains unexplored [15–17]. For this reason, the synthesis and application of new TMDs nanosheets such as 2D-$ReS_2$ and 2D-$TiS_2$ for electrochemical sensor development are interesting strategies in order to clear a path in the analytical chemistry field [18].

The use of colourants in some industries, as alimentary and pharmaceutical, improves the appearance of the foods and drugs. However, their content must be regulated due to their harmful side effects such as hyperactivity, asthma and allergic reactions [19–21]. Azo colourants, as tartrazine (TAR; E−102) and sunset yellow (SY, E−110), are a family of synthetic dyes frequently used in the alimentary industry, both alone or combined, to give a yellow - orange hue to the products. Different analytical methods have been reported in the literature for the determination of these analytes using spectrophotometric techniques, capillary electrophoresis, high performance liquid chromatography combined with different detectors and electrochemical sensors [22–27]. Methodologies based on chromatography have important advantages due to the nature of the separation process, but they require expensive instrumentation. In contrast, the development of electrochemical sensors provides cheap, miniaturized, and selective analytical methodologies. Moreover, when the sensors designed are robust enough to be employed as transducers in flow injection analysis (FIA) systems, on-line methodologies with high sample analysis frequency, in comparison to discontinuous strategies, can be developed with cheap, affordable and simple instrumentation. However, the simultaneous determination of more than one analyte is not possible using a simple amperometric FIA system. The use of flow injection analysis with multiple pulse amperometric detection (FIA-MPA) can overcome this limitation [28]. This strategy is based on the monitorization of the current at two different potential values when consecutive pulses are applied. The methodology is based on the oxidation of only one analyte at the lower pulse potential while, at the highest pulse potential, both analytes are oxidized. In this way, the first analyte can be determined at the lower oxidation potential and the second one from the difference between the currents obtained at both potentials. This methodology has been previously employed for the determination of indigo carmine and allura red as well as caffeine, ibuprofen and paracetamol, among other examples [28,29].

In this work, we have synthetized and characterized nanosheets of $ReS_2$ and $TiS_2$. For the first time, the synergy of these nanosheets with diamond nanoparticles was tested for the design of an electrochemical sensor as transducer in a FIA system with multiple pulse amperometric detection for the simultaneous analysis of sunset yellow and tartrazine.

## 2. Materials and methods

### 2.1. Reagents

The transition metal disulfide nanomaterials (90 nm, 99%), tungsten disulfide (IV), titanium disulfide (IV) and rhenium disulfide (IV) as well as the dyes, sunset yellow (SY) and tartrazine (TAR), were purchased from Sigma-Aldrich (USA). Diamond nanoparticles (4–15 nm diameter) were supplied by SkySpring Nanomaterials (USA). Boric acid, acetic acid, phosphoric acid, sodium hydroxide, ethanol absolute (EtOH) and methanol for HPLC were obtained from Scharlau (Barcelona, Spain). Ultrapure water was used and produced by Milli-Q-system (trademark) of Merk Millipore (Billerica, Massachusetts, USA).

### 2.2. Instruments

Differential Pulse Voltammetry (DPV) measurements were carried out with a potentiostat/galvanostat μ-Autolab Type III with GPES software (Ecochimie, Utrecht, Netherlands). A three electrodes cell was employed using a bare or modified glassy carbon electrode (GCE) as the working electrode, an Ag/AgCl/KCl (3 M) electrode as the reference electrode and a platinum wire as a counter electrode.

The flow injection analysis (FIA) measurements were carried out using a peristaltic pump, Pumpdrive5201 (Brikmann), an injection valve with six ports (Omnifit) and a wall-jet electrochemical detection cell (Metrohm). The amperometric detection was carried out with a modified glassy carbon electrode (GCE/$ReS_2$/DNPs) as a working electrode, an Ag/AgCl/KCl (3 M) electrode as reference electrode and a gold disc as a counter electrode.

High Performance Liquid Chromatography (HPLC) measurements were performed with a Jasco Analytica PU-1580 high pressure pumping system, equipped with an injector Rheodyne Model 7125, a 20 μL loop and a Spherisorb C18 column (250 × 4.6 mm; 5 μm; Scharlau). A PerkinElmer 785 A UV/VIS was employed as detector of the chromatographic system.

An ultrasonic bath Transonic 570/H (Elma Schmidbauer GmbH), a pH meter (Metrohm) and a centrifuge Rotofix 32 A (Hettich) were employed for the preparation of nanomaterials and electrolytes.

The morphological characterization was done using a Nanoscope IIIa (Veeco) equipment operating in the dynamic mode and employing silicon cantilevers (Bruker) with a nominal force constant of 40 N/m and nominal radius of curvature of 8 nm. The Kelvin Force Microscopy (KFM) measurements were performed with an Agilent Picoplus 5500 microscope (Agilent) and using Pt coated tips, model ANSCM-PT-20 (AppNano), with a radius smaller than 40 nm. In these experiments, maps of the topography, contact potential difference (CPD) and gradient of the tip-sample capacitance ($\partial C/\partial z$) are simultaneously obtained. The changes in both the CPD and the gradient of the tip-sample capacitance are related to local changes of the surface potential and of the dielectric constant, respectively [30]. For I–V measurements a Nanobserver microscope and a Resicope module (both from Concept Scientific Instruments, France) were employed using Pt tips (Rocky Mountain Nanotechnology) with a nominal constant force of 18 N/m and tip radius below 20 nm. These data were collected in the soft resiscope mode by applying a voltage ramp to the tip (sample being grounded) while measuring the flowing current, thus obtaining I–V curves.

### 2.3. Procedures

#### 2.3.1. Nanomaterials synthesis

$ReS_2$ and $TiS_2$ nanosheets were synthesized through top-down solvent exfoliation assisted by ultrasounds following previous reports [8,9,31]. Specifically, 75.00 mg of the corresponding TMD in 10.0 mL of EtOH/$H_2O$ (45:55 v/v) were sonicated for 2 h. After 24 h at 4 °C, the resulting mixture was centrifuged at 4000 rpm for 45 min. Finally, the supernatant was separated and stored at 4 °C.

The DNPs suspension was prepared in water reaching a concentration of 1.0 mg/mL. The mixture was treated in an ultrasonic bath for 30 min. The resulting suspension was stored at 4 °C.

#### 2.3.2. Electrode modification

The GCE was modified by drop casting of 6.0 μL of the corresponding TMD suspension and then dried at 45 °C in an oven (GCE/TMDs) for 10 min. Next, over this first layer, 6.0 μL of diamond nanoparticles suspension were added and left to dry at 45 °C (GCE/TMDs/DNPs).

#### 2.3.3. AFM measurements

For the topographical measurements, the samples were prepared on silicon substrates by drop casting 10.0 μL of a 1:10 diluted $ReS_2$ suspension and then dried at 45 °C in an oven (Si/$ReS_2$). Then, over this

first layer, 10.0 μL of 1:10 diluted DNPs suspension were added and left to dry at 45 °C (Si/$ReS_2$/DNPs).

For I–V measurements, the samples were prepared in the same way as the topographical samples by a sequential drop casting of 10.0 μL of the non-diluted TMD and DNPs suspensions. Therefore, the same concentration than that used in the sensing device was employed. After drying, this modification left a visible rounded compact mark on the silicon. Afterwards, a drop of silver dag was deposited connecting the AFM metallic sample-holder and this rounded mark to enable the electrical continuity. Once dried, with the aid of an optical microscope attached to the AFM, the conductive Pt tip was addressed to those locations close to the silver dag where the deposited material was clearly visible. Then a ramp of voltage was applied to the tip (the sample being grounded) and the current was measured. The I–V measurements were made at different locations.

### 2.3.4. Electrochemical measurements

The differential pulse voltammetry scans were carried out between 0.40 V and 1.25 V with a pulse amplitude of 80 mV and a scan rate of 30 mV/s (pulse potential of 0.015 V and an interval time of 0.5 s).

FIA measurements were carried out using acetic acid/sodium acetate buffer (0.1 M, pH 5) as carrier solution at a constant flow of 3 mL/min. When a stable signal was obtained, the sample was injected into the flow with a 6 ports injection valve and a sample loop of 250 μL. The multiple pulse amperometric detection (FIA-MPA) was carried out by applying continuously potential pulses of 0.8 V and 1.2 V in steps of 250 ms of pulse time.

### 2.3.5. HPLC-UV measurements

HPLC-UV measurements were performed with a mobile phase of ammonium acetate (0.02 M)/MeOH (35/65 v/v) with a flow rate of 0.7 mL/min and a detection wavelength of 461 nm.

### 2.3.6. Sample preparation

A pineapple-flavoured jelly powder, purchased from a local store, containing both dyes, was employed as a real sample. Before the measurement, an extraction treatment was carried out following a previous published procedure [32]. A mass of 5.0000 g of jelly was extracted successively with 10.0 mL of methanol and acetone until the jelly powder lost its color. Afterwards, the extract was centrifuged in order to remove any powder that could remain after the successive extractions. After the separation of the supernatant, the solvent was evaporated by applying heat under $N_2$ flow. The resulting residue was reconstituted in 5.0 mL with methanol. An aliquot of 0.75 mL of sample was diluted to 5.0 mL with the carrier solution and injected in the FIA-MPA system. Different aliquots of 0.75 mL of sample were spiked with increasing concentration of both analytes and, after dilution to 5.0 mL, were injected in the FIA-MPA system.

For HPLC analysis, 300 μL of the sample extract were diluted with the mobile phase to 5.00 mL before filtration through a 0.45 μm pore size filter and subsequent injection.

## 3. Results and discussion

### 3.1. Optimization of the sensor design

In previous works, we have demonstrated the synergistic effect produced when combining $WS_2$ nanosheets and DNPs in the design of electrochemical sensors [8,9]. In this work, $TiS_2$ and $ReS_2$ were selected in order to evaluate the influence of the nature of the transition metal on the electrochemical response of the sensor for the simultaneous determination of sunset yellow (SY) and tartrazine (TAR). Moreover, the comparison of the performance of these new 2D-TMDs materials in contrast with the use of 2D-$WS_2$ is also included. Fig. 1 shows the differential pulse voltammetry response of a mixture of both analytes with GCE electrodes modified with hybrids of each TMD ($WS_2$, $ReS_2$ or $TiS_2$) and DNPs. In addition, the response obtained with the bare GCE is also included for comparison. As observed with the bare GCE (curve a), two anodic peaks are recorded. These peaks, at 0.72 V and 0.95 V, are ascribed to the oxidation of SY and TAR, respectively. This assignment is performed by comparing the response obtained for SY and TAR in individual solutions with that obtained in a mixture of both (see Figure S1). The separation between both anodic peaks ($\Delta E_p \geq 0.2$ V) is large enough to afford their simultaneous determination in a FIA-MPA system.

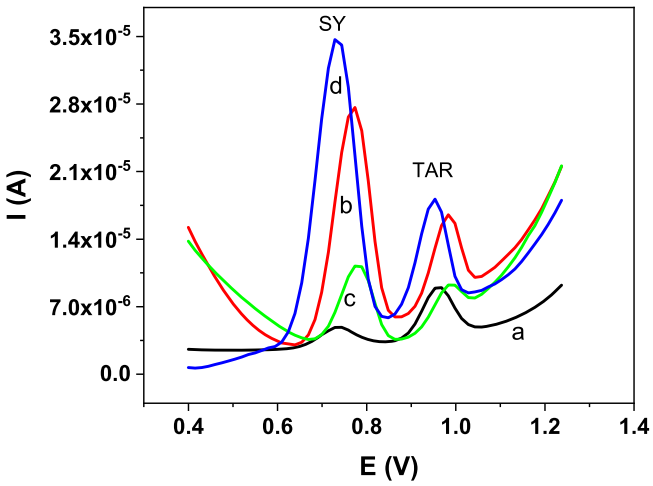


**Fig. 1.** Differential pulse voltammetry response of a SY and TAR mixture solution with a) GCE, b) GCE/$WS_2$/DNPs, c) GCE/$TiS_2$/DNPs and d) GCE/$ReS_2$/DNPs. Acetic acid/acetate buffer solution 0.1 M pH 5. [SY] = $10^{-5}$ M, [TAR] = $10^{-5}$ M.

When analysing the response using the different sensors (GCE/TMD/DNPs with TMD = $WS_2$, $TiS_2$ or $ReS_2$), it is observed that in all cases the modification of the electrode with both layers (TMD/DNPs) produces an increase in the current intensity with respect to the unmodified electrode. These results are in good agreement with previous studies involving the use of GCE/$WS_2$/DNPs sensors [8,9] and allow us to conclude that such an effect is not exclusive of $WS_2$ or $MoS_2$ but is also produced by other TMDs. Moreover, our results reveal the influence of the nature of the transition metal of the TMD, since as it can be seen by comparing lines b, c and d in Fig. 1, the extent of the intensity increment with respect to the bare GCE depends on the TMD. As observed in Fig. 1 line c, the GCE/$TiS_2$/DNPs sensor leads to the lowest increase in the oxidation current, which becomes almost negligible in the case of TAR. In contrast, for GCE/$WS_2$/DNPs (curve b) and GCE/$ReS_2$/DNPs (curve d), a higher increment in the peak current with respect to the unmodified electrode for both SY and TAR is produced. Moreover, for the GCE/$ReS_2$/DNPs (curve d) system, a shift towards lower potential values is also observed, which is advantageous in terms of selectivity. Therefore, the GCE/$ReS_2$/DNPs sensor offers the best analytical response, leading to the highest peak currents and the lowest peak potential values, improving both the sensitivity and the selectivity of the method. These results aimed us to pursue the rest of the experiments with $ReS_2$ as TMD nanomaterial.

To ensure that the enhanced response is due to the synergistic effect between $ReS_2$ nanosheets and DNPs, the modification of the electrode surface was carried out with each nanomaterial independently. The results, displayed in Fig. 2, show that the presence of $ReS_2$ on the electrode surface (curve b) produces a decrease in the current intensity of both analytes. This was the typical behavior observed when electrodes were modified just with sheets of $MoS_2$ or $WS_2$ and it can be attributed to the semiconducting properties of the TMD [1,9,11]. On the contrary, the GCE/DNPs electrode (curve c) produces an increase in the current and a slight peak potential shift towards lower values due to the high conductivity and catalytic properties exhibited by this carbon nanomaterial.

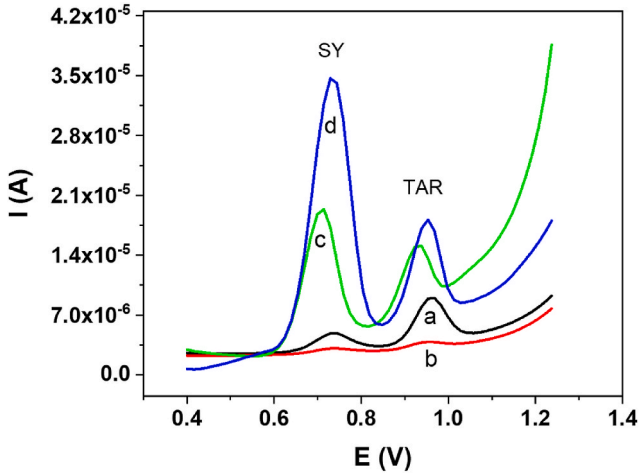


**Fig. 2.** Differential pulse voltammograms of SY and TAR with a) GCE, b) GCE/$ReS_2$, c) GCE/DNPs and d) GCE/$ReS_2$/DNPs. Acetic acid/acetate buffer solution 0.1 M pH 5. [SY] = $10^{-5}$ M, [TAR] = $10^{-5}$ M.

As can be observed, the combination of both nanomaterials on the electrode surface produces the highest increase in the intensity, showing that the synergistic effect obtained previously with $WS_2$ is maintained with $ReS_2$ (curve d). The layered structure of the TMD provides a higher electrochemical surface for the incorporation of the DNPs which provide catalytic properties.

### 3.2. AFM characterization of the sensor surface

Once we have selected GCE/$ReS_2$/DNPs as the more adequate platform to detect SY and TAR, we proceeded to characterize the surface resulting after each step of the sensor construction. As observed in Fig. 3A, the Si/$ReS_2$ was characterized by the presence of a network of flakes that, in some zones, practically cover the surface. The plateau surface is very flat, with rms roughness of 0.5 nm, although it displays some bumps or nanoprotuberances with a height of 0.5 nm. The arrow in Fig. 3B indicates these protuberances on a plateau. Regarding the thickness of the flakes, Fig. 3B shows the surface profile along the line marked in Fig. 3A. The thickness can be estimated to be close to 3 nm.

Next, we studied by AFM the Si/$ReS_2$/DNPs sample. Fig. 4A shows the typical morphology at the nanoscale. Here, in the background, flakes scattered on the silicon surface, with a thickness close to 3 nm, are imaged. In this case, the flakes do not form a network, as in Fig. 3A, but they are isolated. About at the middle of the image large structures, 40–60 nm high, are observed, which are indicated by arrows. A detailed inspection shows that they are composed by the aggregation of different rounded structures that correspond to the DNPs, which tend to gather together [31,33].

In Fig. 4B, a zoom of the surface of a large flake is shown. The interest of this image is that different height levels corresponding to individual flakes can be distinguished. Thus, a sort of multilayer flake structure is obtained. In fact, the height distribution of this image, shown in Fig. 4C, displays different peaks. Note that the x-axis of this histogram corresponds to the height level, and the y-axis to the normalized amount of locations (i.e., pixels) with a given height. In this sense, the different peaks come from the different terraced flake structures that provide with enough pixels to have a relative high frequency in the graph. The most noticeable aspect of this plot is that the x-axis (height) distance between peaks, going from left to right, are 2.3 nm, 2 nm, 3.6 nm, 3.4 nm and 1.4 nm. Within the experimental error, all these values are close to multiples of 0.7 nm, which is the thickness of a single monolayer of $ReS_2$ [34].

In order to further characterize the Si/$ReS_2$/DNPs sample, we also performed KFM measurements. In these experiments, as described in the experimental section, we obtained simultaneously the maps of the topography, CPD and gradient of the capacitance, which could then be correlated. Such images are shown in Fig. 5A, B and C, respectively. The topographical image (Fig. 5A) shows a wide area where the flakes also form a sort of compact network although the whole surface is not covered by it (see particularly the bottom left corner). Scattered on top of this layer different structures are imaged. Particularly, at the top half left part of the image many tiny structures, 5–8 nm high, are found. These could correspond either to $ReS_2$ small structures or to tiny DNPs. The large structures, with heights in the 50–100 nm range, clearly correspond to aggregates of DNPs, as in many cases the individual nanoparticles can be distinguished. Five of these protuberances are numbered in the different images in order to clearly correlate the different data. Precisely, these large DNPs structures are those that yield higher contrast in the capacitance gradient image, as they appear with a dark hue. This sort of contrast was already found in other sensing systems containing DNPs [7].

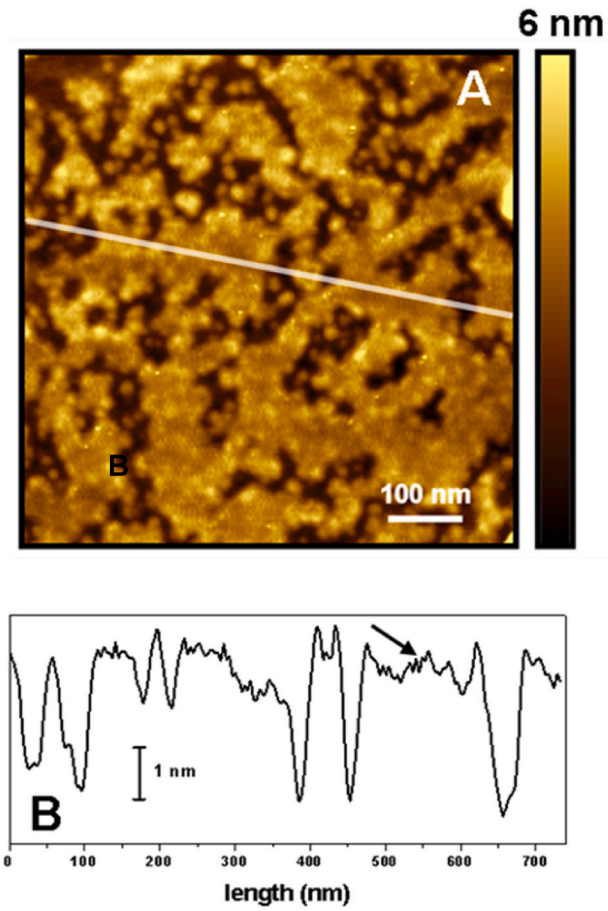


**Fig. 3.** (A) AFM image of the Si/$ReS_2$ sample. The long line indicates the section to which corresponds the surface profile depicted in (B). In this profile, the nano-protuberances on a plateau are indicated with an arrow.

In the CPD map, however, the contrast is more homogeneous. It seems that the $ReS_2$ gives a slightly higher contrast than the substrate, around 20 mV higher. Likewise, the largest DNPs structures also give higher (brighter) contrast. These correlations are better shown in the plots of Fig. 5D that display the profiles along the long line in the three images. There, it is obvious that the DNPs protrusions yield less contrast in the gradient of capacitance and only the largest ones give higher contrast in the CPD plot. Most of the tiny structures observed at the top left part of the topography (see above) yield a slight dark gradient capacitance contrast, which suggests that they likely are small DNPs.

Finally, we have studied the conductive properties of the $ReS_2$ and $ReS_2$/DNPs samples by performing measurements of I–V curves using a

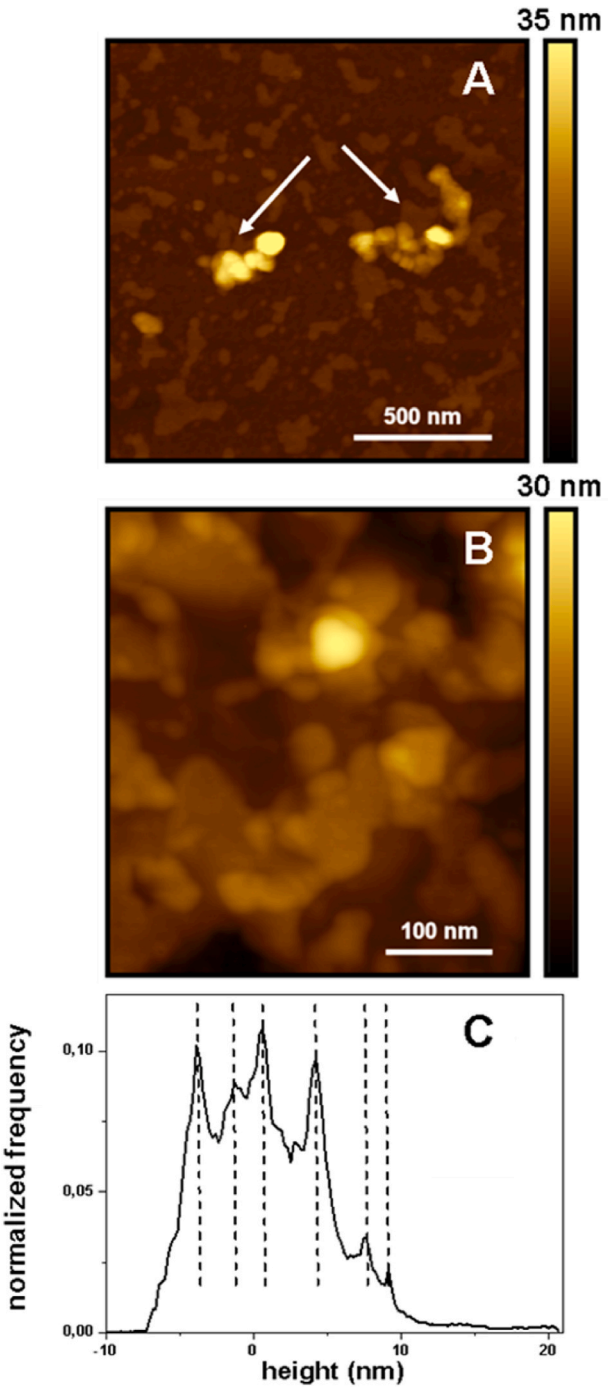


**Fig. 4.** (A) AFM image of the Si/$ReS_2$/DNPs sample. The arrows show the DNP aggregated structures. (B) Zoomed image on top of a $ReS_2$ flake. (C) Height distribution corresponding to (B). The peaks correspond to the height levels (x-axis) of the different terraces.

Pt tip with AFM operating in the soft resiscope mode (see Experimental).

Fig. 6 displays characteristic I–V curves obtained in these measurements. The Ag reference gives an ohmic behavior. In contrast, the curves obtained for the $ReS_2$ and $ReS_2$/DNPs samples show a different behavior where a gap is detected at low voltages. The curve displayed for $ReS_2$ is characteristic of this sample. It shows a gap of ~0.2 V, which is smaller than the expected value of 1 V [35]. Probably, the high number of defects associated to the preparation method as well as the contact effects between the metal (silver or Pt) and $ReS_2$ may account for the observed changes in the gap value and curve shape [35–37]. The curves displayed for the $ReS_2$/DNP system have been taken on different locations close to the silver dag. Although the shape is maintained, and similar to that obtained for the $ReS_2$ sample, the gap value changes with the location. It can be very similar to that of $ReS_2$ and appreciably smaller. It should be noted that the presence of C–H bonds at the DNP surface can reduce both its bandgap and resistivity [38–40]. In addition, the control over the specific location on which the I–V curves are taken is in the several microns range, which implies that for the $ReS_2$/DNPs sample the curves can be measured at spots either free or rich of DNPs.

### *3.3. Optimization of the FIA-MPA methodology for simultaneous TAR and SY determination*

Once $ReS_2$ was selected to be combined with DNPs and the resulting surface was morphologically characterized, the influence of the pH of the electrolyte on the electrochemical performance was studied under static conditions. Thus, a mixture of both analytes was measured at different pH values and the results are shown in Figure S2. As expected, the peak potential corresponding to the oxidation of both analytes shifts towards lower values as pH increases according to the Nernst equation (see Figure S2B). The slopes values of −0.033 V/pH and −0.029 V/pH obtained for SY and TAR respectively, show that, in both electrochemical processes, the number of electrons involved is twice the number of protons. Similar results have been reported in the literature for these analytes [41,42]. In addition, at pH values higher than 9.0, the peak corresponding to TAR oxidation disappears, while for both additives, good responses were obtained at pHs lower than 5. At pH 2, the current obtained for TAR is higher than at pH 5, which is just the opposite case than for SY, where the highest intensity is recorded at pH 5. In order to select between pH 2 and pH 5, two aspects were taken into account, namely the current values and peak potentials obtained for each colorant. Currents are high enough for both pH conditions. However, lower potential values are required for the determination of SY and TAR at pH 5. Accordingly, in a compromise between sensitivity and selectivity, acetic acid/acetate pH 5 was selected as electrolyte to be employed as carrier in the flow injection analysis method.

Since this kind of modification based on TMD/DNPs was never employed before in FIA systems, it was necessary to evaluate its robustness and stability under flow conditions. Therefore, the response of the GCE/$ReS_2$/DNPs was evaluated in a FIA with a single amperometric detection system. The response of each dye was registered with both the GCE and GCE/$ReS_2$/DNPs sensors by applying the corresponding potential value for the oxidation of each analyte obtained from the differential pulse voltammetry measurements: 0.72 V for SY and 0.95 V for TAR. In agreement with the results previously obtained in batch measurements, in both cases the modified electrode offers higher currents than those obtained with the unmodified one (Figure S3). Moreover, although the fiagrams recorded with the GCE/$ReS_2$/DNPs show wider peaks than with the unmodified electrode, the reproducibility of the signals in successive measurements, especially in the case of TAR oxidation, is much better when the developed sensor is used as a detector. So, it could be concluded that the GCE/$ReS_2$/DNPs is stable enough to work under flow conditions.

Next, we optimized all the parameters affecting the analytes response in the FIA-MPA system. The potentials to be applied for the detection of each compound and the duration of the potential pulses were evaluated. To this end, the hydrodynamic curves were recorded (Figure S4). For SY, the current increased sharply while increasing the applied potential up to 0.9 V, and then slowly until reaching a maximum value at 1.0 V. For TAR, the current increased up to 1.1 V, and then remained nearly constant for higher potential values. For the simultaneous FIA-MPA determination, it is required that at the first potential pulse applied, only one of the analytes is oxidized. Based on this criterion, a first potential pulse of 0.8 V was selected for SY determination since at higher potentials the oxidation of TAR begins to become significant. A value of 1.2 V was selected as second pulse potential since a maximum intensity is recorded

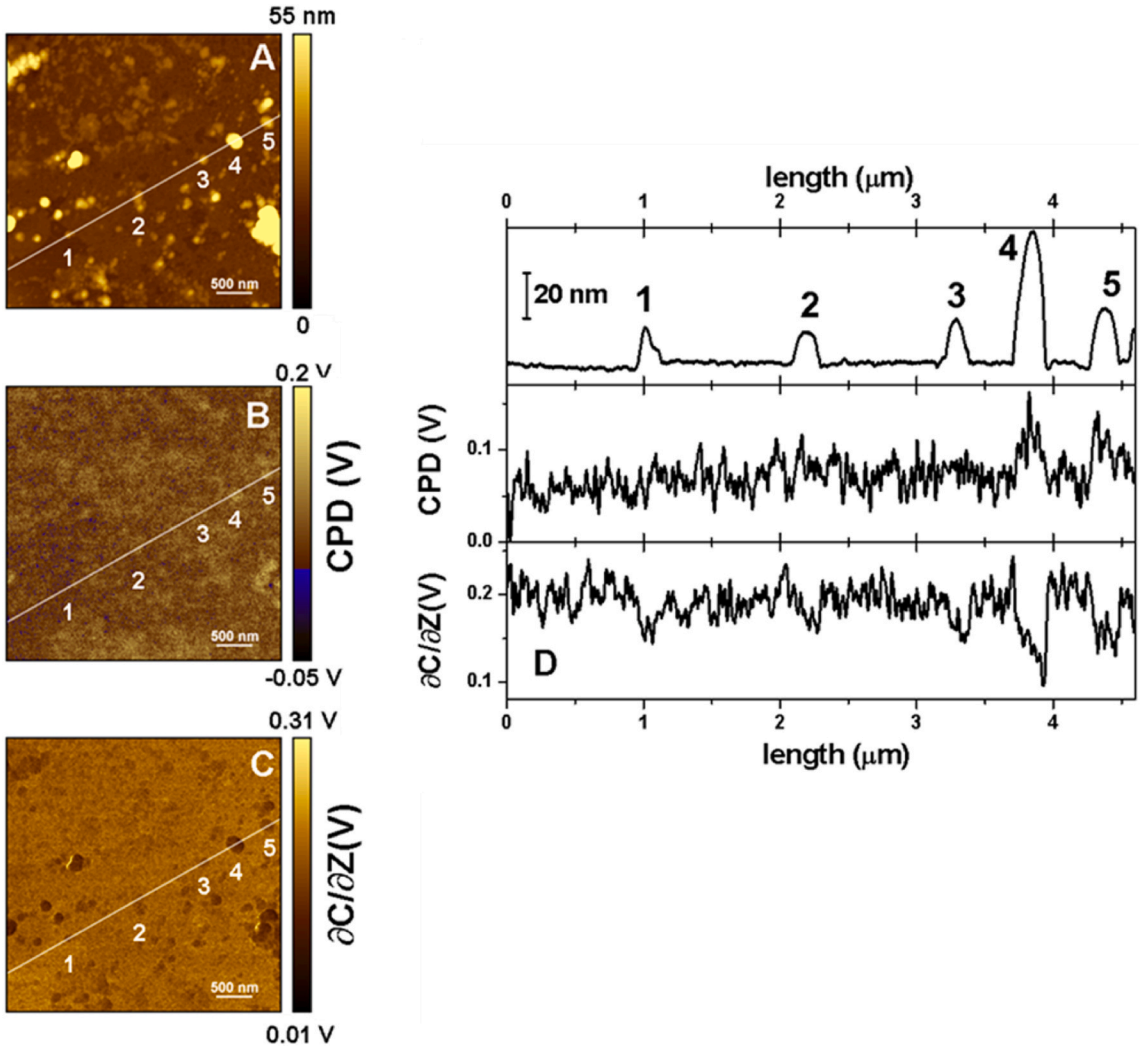


**Fig. 5.** Left column: (A) Topographical map, (B) CPD map and (C) ∂C/∂z map measured simultaneously. Right column: (D) Corresponding profiles along the long line depicted in the left column images. The numbers 1 to 5 indicate protuberances in the topography and their corresponding locations in the CPD and ∂C/∂z maps. They are also marked on the top topographic profile.

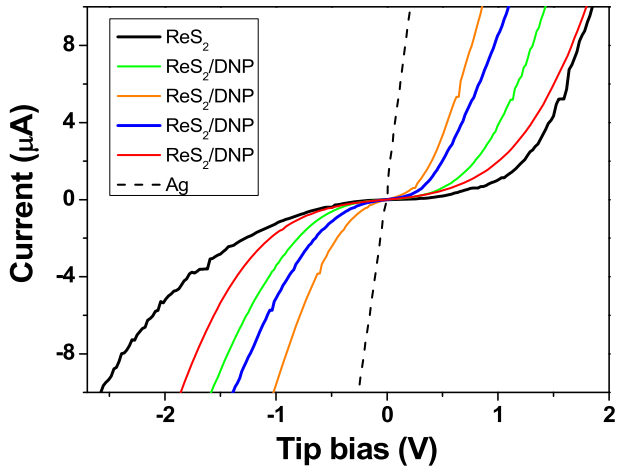


**Fig. 6.** I–V curves obtained on the silver dag reference (dashed line), the $ReS_2$ surface (black solid line) and $ReS_2$/DNPs sample (color solid lines) with a Pt tip. The color solid curves correspond to different locations.

for TAR.

The duration of the potential pulses was optimized following the same criteria mentioned above. To this end, the currents of both analytes were monitored varying the potential pulses between 100 and 250 ms (data not shown). The best results were obtained for 250 ms as the signal of SY at 0.8 V had the highest current intensity while the oxidation current of TAR remained almost negligible being, consequently, its contribution at this lower potential insignificant.

Fig. 7 shows the electrochemical response of SY, TAR and a mixture of both under the selected conditions. As can be observed, at $E_1 = 0.8$ V, only SY is oxidized while the current for TAR is insignificant. However, at $E_2 = 1.2$ V both SY and TAR are oxidized. Thus, the quantification of SY can be carried out with the current recorded at $E_1$ ($I_{SY} = I_{E1}$), whereas for TAR determination, a subtraction of both currents is required ($I_{TAR} = I_{E2} - I_{E1}$).

Next, the carrier flow rate and the sample injection volume were also studied in order to obtain the best analytical performance of the methodology. Both studies were carried out injecting a solution containing a mixture of SY and TAR with $5.0 \times 10^{-5}$ M and $2.5 \times 10^{-5}$ M concentration, respectively. For the flow rate study, the current was monitored varying the flow rate between 1 and 4 mL/min. As expected, higher flow rate values produced an increase in the peak intensity response together with wider FIA peaks that affect the sample frequency. In a compromise

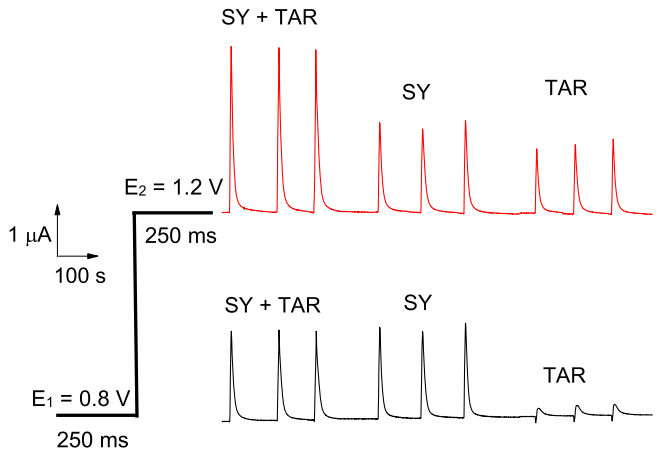


**Fig. 7.** Potential pulse scheme and FIA-MPA response of SY, TAR and SY + TAR with GCE/$ReS_2$/DNPs sensor. Carrier solution of acetic acid/acetate buffer 0.1 M pH 5 at 3.0 mL/min. Sample injection volume of 100 μL.

between sensitivity and sample frequency, 3 mL/min was selected as the flow rate for the rest of the experiments.

For the optimization of the volume injection, the volume of the loop was varied between 25 μL and 500 μL. As before, as the sample volume increases, the current intensity increases until reaching a maximum with a sample volume of 300 μL. The increase in the volume also produces wider peaks that affect the sample frequency. A volume of 250 μL was selected as optimal and, under these optimized conditions, a sampling frequency of 66 samples per hour was obtained.

### *3.4. Influence of SY and TAR concentration: calibration graph and analytical parameters*

Once all the FIA-MPA parameters were optimized, the influence of each analyte concentration in the electrochemical response was evaluated by the injection of mixtures with different concentration levels. Fig. 8 shows an increase in the oxidation current with increasing concentrations of each analyte at both potentials. For the SY determination, the current increased linearly between $1.00 \times 10^{-6}$ and $8.75 \times 10^{-5}$ M as given by the equation Ip (A) = $(7.3 \pm 4.5) \times 10^{-8} + (4.20 \pm 0.10) \times 10^{-2}$ [SY] (M); r = 0.998. For TAR, the linear range was found between $7.50 \times 10^{-7}$ and $8.75 \times 10^{-5}$ M according with the equation Ip (A) =

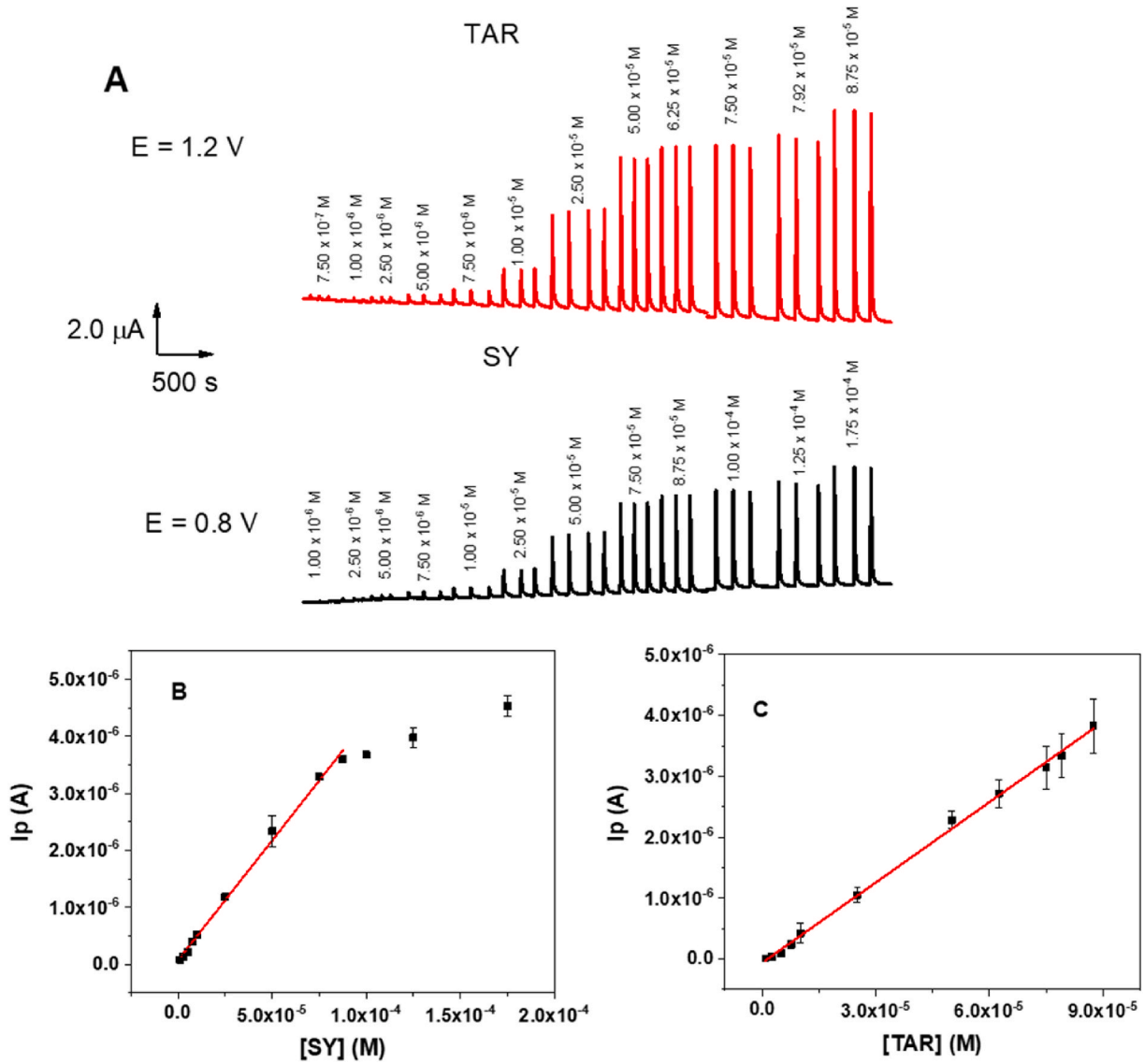


**Fig. 8.** (A) FIA-MPA response for increasing concentrations of SY and TAR using a GCE/$ReS_2$/DNPs sensor. (B) and (C) are the corresponding calibration curves.

$(-5.4 \pm 3.7) \times 10^{-8} + (4.385 \pm 0.072) \times 10^{-2}$ [TAR] (M); r = 0.998.

The detection (3σ/slope) and the determination limits (10σ/slope) obtained were $3.51 \times 10^{-7}$ M and $1.17 \times 10^{-6}$ M for the determination of SY and $2.39 \times 10^{-7}$ M and $7.98 \times 10^{-7}$ M for TAR. Table 1 shows some examples reported in the literature for the simultaneous determination of TAR and SY. Lower detection limits can be reached when the electrochemical sensor is working in a batch system. However, if the results are compared to the only work employing a FIA-MPA system, the detection limits obtained in our work are lower. For some applications, reaching very low detection limits is important. However, this is not necessary for the analysis of dyes in food samples because their concentrations are usually high enough. In this kind of samples, it is important to be able to determine a high number of samples in a short amount of time. With our method, we have found a sampling frequency of 66 samples per hour.

The accuracy and the precision (in terms of reproducibility) of the methodology were also evaluated. These parameters were calculated in terms of relative errors (Er %, n = 3) and relative standard deviations (RSD %, n = 3), obtaining values lower than 12.6% and 7.8%, respectively. The study of the stability of the sensor in the FIA-MPA system was performed by the successive injections of a mixture of SY and TAR with $2.5 \times 10^{-5}$ M and $1.00 \times 10^{-5}$ M concentrations, respectively. Figure S5 shows the response of the GCE/$ReS_2$/DNPs sensor during 50 consecutive measurements. The horizontal bars represent the limit values established with 10% of signal variability as criterion. The results show the high stability of the signal during the experiment with a RSD (n = 50) of 2.9% and 3.6% for SY and TAR, respectively. These results demonstrate that the current remained constant during at least 50 measurements, allowing us to conclude that, even when working under flow conditions, the modification of the glassy carbon electrode surface with $ReS_2$ and DNPs remains stable, without becoming detached in the solution.

### 3.5. Interferences

The study of the influence of other substances that could alter the signal of the analytes under investigation was carried out. The interferents included in this study were compounds that are usually present in the sample with the analytes. For this, a mixture of SY ($2.5 \times 10^{-5}$ M) and TAR ($1.0 \times 10^{-5}$ M) without and with increasing concentration of the corresponding interferent were injected in the FIA-MPA system and the intensity current was recorded. It was considered that an interference is produced when the analytical signal of each compound changes by more than a 10% of the initial current of SY and TAR in the mixture. Table 2 includes the maximum allowed concentration and the corresponding change in the intensity for each assayed interference (sodium chloride, sodium citrate, glucose and fructose).

From the results, the maximum interference was produced by fructose for both SY and TAR, since the concentrations of the interferents are 5-fold and 2-fold lower than the SY and TAR concentrations, respectively. In contrast, NaCl does not produce any interference up to $5.00 \times 10^{-4}$ M, which represents a 20-fold and 50-fold concentration level with respect to SY and TAR, respectively. Therefore, we have shown that the sensor has an adequate selectivity with respect to compounds that are typically present in food samples containing both dyes.

**Table 1**
Comparative methods for TAR and SY determination. AuNPs/PDDA-Gr/GCE: poly (diallyldimethylammonium chloride) functionalized gold nanoparticles/graphene/glassy carbon electrode. GN/$TiO_2$-CPE: Graphene and mesoporous $TiO_2$ modified carbon paste electrode. HPLC-DAD: High performance liquid chromatography-diodo array detector. ERGO-AuNRs/GCE: electro-reduced gold nanorods decorated graphene oxide on glassy carbon electrode. β-CD-PDDA-Gr/GC-RDE: β-cyclodextrin-coated poly (diallyldimethylammonium chloride)-functionalized graphene composite film modified glassy carbon-rotating disk electrode. MWCNTs–IL/CCE: Carbon nanotube-ionic liquid nanocomposite modified sol-gel derived carbon-ceramic electrode. BDD: Boron-doped diamond electrode. DPV: Differential pulse voltammetry. SWV: square wave voltammetry.

| Method | SY $_{LOD}$ (μM) | TAR $_{LOD}$ (μM) | Reference |
|---|---|---|---|
| AuNPs/PDDA-Gr/GCE (DPV) | 0.002 | 0.0025 | [43] |
| GN/$TiO_2$-CPE (SWV) | 0.006 | 0.008 | [44] |
| HPLC-DAD | 0.049 | 0.019 | [45] |
| ERGO-AuNRs/GCE (DPV) | 0.0024 | 0.0086 | [46] |
| β-CD-PDDA-Gr/GC-RDE (DPV) | 0.120 | 0.140 | [47] |
| MWCNTs–IL/CCE (DPV) | 0.11 | 1.100 | [48] |
| BDD (FIA-MPA) | 2.5 | 0.8 | [49] |
| GCE/$ReS_2$/DNPs | 0.35 | 0.24 | This work |

**Table 2**
Maximum allowed concentration and ΔIp produced by other compounds in SY and TAR determination.

| Interference | Maximum allowed concentration (M) | ΔIp (0.8 V) (%) | ΔIp (1.2 V) (%) |
|---|---|---|---|
| Sodium chloride | $5.00 \times 10^{-4}$ M | 9.7 | 12.4 |
| Sodium citrate | $1.00 \times 10^{-5}$ M | 9.4 | 9.7 |
| Glucose | $7.50 \times 10^{-5}$ M | 10.4 | 9.8 |
| Fructose | $5.00 \times 10^{-6}$ M | 9.2 | 9.5 |

### 3.6. Analytical application: determination of SY and TAR in pineapple jelly

The sensor was applied in the determination of both analytes in a pineapple-flavoured jelly purchased in a local shop. As stated in the procedure section, a sample of 5.0000 g was weighted, successively extracted and finally reconstituted in 5.0 mL of methanol. An aliquot of extract of 750 μL was diluted to 5.00 mL with carrier solution and then injected in the FIA-MPA system. The standard addition method was employed to carry out the analytical determination. Fig. 9 shows the FIA-MPA response of the sample solution before and after adding increasing concentrations of TAR and SY. The current intensity varies linearly with the concentration of the standard added, according to equations Ip (A) = $6.5 \times 10^{-7} + 3.5 \times 10^{-2}$ [SY] (M); r = 0.990 and Ip (A) = $4.8 \times 10^{-7} + 5.7 \times 10^{-2}$ [TAR] (M); r = 0.990 for SY and TAR, respectively. After the corresponding extrapolation, the average concentration calculated in the measured solution is $1.86 \times 10^{-5}$ M for SY and $8.42 \times 10^{-6}$ M for TAR, which results in concentrations of $1.24 \times 10^{-4}$ M and $5.6 \times 10^{-5}$ M in the sample, respectively. From these data, values of 53.7 mg/kg of SY and 29.0 mg/kg of TAR were obtained,

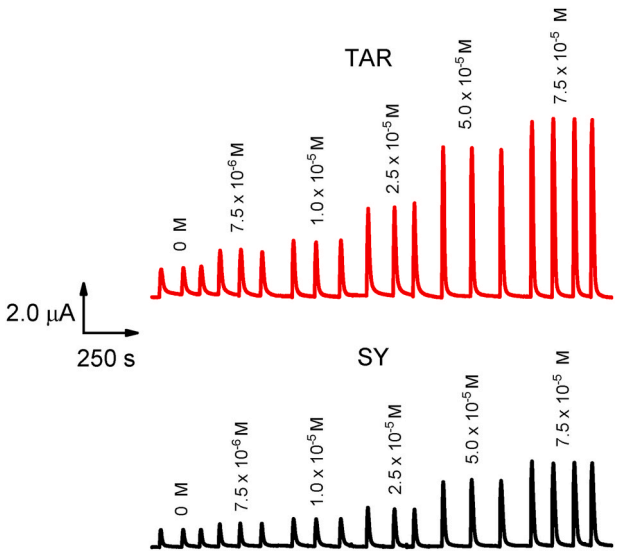


**Fig. 9.** FIA-MPA response of the sample solution before and after adding increasing concentrations of TAR and SY.

which are lower than the maximum legal amounts stablished by the European Union for these kinds of samples [50]. By comparing the slopes obtained by the addition standard method and the external calibration employing the *t*-test, values of $t_{calc} = 5.43$ for SY and $t_{calc} = 3.75$ for TAR and $t_{tab}$ (4, 0.95) = 2.78 were obtained. Therefore, as the slopes are significantly different, the need for using the addition standard method instead of the external calibration was verified. Finally, in order to evaluate the recovery of the method, we proceeded to analyse spiked samples with a concentration of $7.5 \times 10^{-6}$ M and following the same sample procedure. Taking into account the concentration found in the undoped sample, recovery values of 94% and 105% were obtained for SY and TAR, respectively.

In order to validate the result obtained by the FIA-MPA system, the powder for the preparation of the jelly was further analyzed by HPLC-UV–Vis detection. Figure S6 shows the increase of the signal with colorant concentration according to the following equations: Area = $(-9.8 \pm 4.7) \times 10^3 + (6.53 \pm 0.09) \times 10^4$ [SY] (mg/L) and Area = $(-1.0 \pm 0.7) \times 10^4 + (4.7 \pm 0.1) \times 10^4$ [TAR] (mg/L). Note that TAR and SY were detected at a retention times ($t_R$) of 2.7 and 4.1 min, respectively.

Next, 20 μL of jelly samples, after the treatment described in procedures, were injected in the chromatographic system (see chromatogram in red in Figure S6). From the interpolation of the signals obtained at 2.7 and 4.1 min in the corresponding calibration curves, SY concentration of 56.1 ± 0.7 mg/kg (n = 3) and TAR concentration of 30.0 ± 0.4 mg/kg (n = 3) were obtained. These results are in very good agreement with those found with the proposed FIA method, thus allowing us to confirm that the herein reported method works for routine determination of these food additives in real samples.

## 4. Conclusions

We have developed a new electrochemical sensor based on 2D-$ReS_2$&DNPs as transducer of a FIA-MPA system for the simultaneous determination of SY and TAR. We show that the combined use of $ReS_2$ and DNPs leads to a greater synergistic effect than those achieved with other combinations, where $ReS_2$ is replaced by either $TiS_2$ or $WS_2$. The surface sensor, characterized by AFM and KFM, is formed by scattered and stacked $ReS_2$ flakes, with an individual thickness of around 3 nm, as well as by larger structures compatible with aggregations of DNPs. From local probe (AFM) I–V measurements, gaps close to 0.1 and in the 0.1–0.6 V range are obtained for $ReS_2$ and $ReS_2$/DNPs, respectively. The simultaneous determination of both dyes with the FIA-MPA system is possible thanks to the clear difference in the potential values required for oxidation of SY and TAR (0.8 V and 1.2 V, respectively) and to the fact that only SY is oxidized at the lowest potential pulse applied. Values of pH 5, flow rate 3 mL/min and volume injection of 250 μL were selected as optimum values for the determination. The developed methodology leads to detection limits of $3.51 \times 10^{-7}$ M and $2.39 \times 10^{-7}$ M for SY and TAR, respectively Furthermore, a high sampling frequency of 66 samples per hour was achieved. The modified surface is robust enough to allow at least 50 consecutive measurements with an RSD lower than 3.6%. Finally, the method was applied to the simultaneous determination of both dyes in a pineapple-flavoured jelly sample with good results.

## Credit author statement

**Ricardo Garsed:** Investigation and Formal Analysis, **Luis Vázquez:** Investigation, Formal Analysis and Writing- Reviewing and Editing, **Elena Casero:** Visualization, Writing -Original Draft and Reviewing and Editing and Project Administration, **María Dolores Petit-Dominguez:** Writing- Reviewing and Editing, **Carmen Quintana:** Conceptualization, Visualization, Supervision, Writing -Original Draft and Review and Editing and Project administration, **María del Pozo:** Conceptualization, Investigation, Formal Analysis, Visualization, Supervision and Writing -Original Draft and Review and Editing.

## Declaration of competing interest

The authors declare that they have no known competing financial interests or personal relationships that could have appeared to influence the work reported in this paper.

## Data availability

Data will be made available on request.

## Acknowledgments

The authors acknowledge financial support from projects PID2020-113142RB-C21 and PID2020-113142RB-C22 and TED2021-129416 A-I00 funded by MCIN/AEI/10.13039/501100011033 and P2018/NMT-4349 (TRANSNANOAVANSENS-CM) funded by the Comunidad Autónoma de Madrid. We thank L. Chico for fruitful discussions.

## Appendix A. Supplementary data

Supplementary data to this article can be found online at https://doi.org/10.1016/j.talanta.2023.124842.

## References

[1] A. Sinha, Dhanjai, B. Tan, Y. Huang, H. Zhao, X. Dang, J. Chen, R. Jain, $MoS_2$ nanostructures for electrochemical sensing of multidisciplinary targets: a review, TrAC, Trends Anal. Chem. 102 (2018) 75–90, https://doi.org/10.1016/j.trac.2018.01.008.

[2] A. Gupta, T. Sakthivel, S. Seal, Recent development in 2D materials beyond graphene, Prog. Mater. Sci. 73 (2015) 44–126, https://doi.org/10.1016/j.pmatsci.2015.02.002.

[3] W. Choi, N. Choudhary, G.H. Han, J. Park, D. Akinwande, Y.H. Lee, Recent development of two-dimensional transition metal dichalcogenides and their applications, Mater, Today Off. 20 (2017) 116–130, https://doi.org/10.1016/j.mattod.2016.10.002.

[4] J. Sun, X. Li, W. Guo, M. Zhao, X. Fan, Y. Dong, C. Xu, J. Deng, Y. Fu, Synthesis methods of two-dimensional MoS2: a brief review, Crystals 7 (2017) 198, https://doi.org/10.3390/cryst7070198.

[5] J.N. Coleman, M. Lotya, A. O'Neill, S.D. Bergin, P.J. King, U. Khan, K. Young, A. Gaucher, S. De, R.J. Smith, I. V Shvets, S.K. Arora, G. Stanton, H.-Y. Kim, K. Lee, G.T. Kim, G.S. Duesberg, T. Hallam, J.J. Boland, J.J. Wang, J.F. Donegan, J. C. Grunlan, G. Moriarty, A. Shmeliov, R.J. Nicholls, J.M. Perkins, E.M. Grieveson, K. Theuwissen, D.W. McComb, P.D. Nellist, V. Nicolosi, Two-dimensional nanosheets produced by liquid exfoliation of layered materials, Science 80 (331) (2011) 568–571, https://doi.org/10.1126/science.1194975.

[6] M.T. Rahman, R. Kumar, M. Kumar, Q. Qiao, Two-dimensional transition metal dichalcogenides and their composites for lab-based sensing applications: recent progress and future outlook, Sensors Actuators, A Phys. 318 (2021), 112517, https://doi.org/10.1016/j.sna.2020.112517.

[7] E. Blanco, L. Rocha, M. del Pozo, L. Vázquez, M.D. Petit-Domínguez, E. Casero, C. Quintana, A supramolecular hybrid sensor based on cucurbit[8]uril, 2D-molibdenum disulphide and diamond nanoparticles towards methyl viologen analysis, Anal. Chim. Acta 1182 (2021), https://doi.org/10.1016/j.aca.2021.338940.

[8] E. Blanco, L. Arias, L. Vázquez, M. del Pozo, L. Sánchez, M.D. Petit-Domínguez, C. Quintana, E. Casero, Sensor based on diamond nanoparticles and $WS_2$ for ponceau 4R and tartrazine determination: influence of green solvents employed for $WS_2$ exfoliation, FlatChem 23 (2020), 100185, https://doi.org/10.1016/j.flatc.2020.100185.

[9] E. Blanco, L. Hristova, R. Martínez-Moro, L. Vázquez, G.J. Ellis, L. Sánchez, M. del Pozo, M.D. Petit-Domínguez, E. Casero, C. Quintana, A 2D tungsten disulphide/diamond nanoparticles hybrid for an electrochemical sensor development towards the simultaneous determination of sunset yellow and quinoline yellow, Sensor. Actuator. B Chem. 324 (2020) 1287, https://doi.org/10.1016/j.snb.2020.128731.

[10] M. del Pozo, C. Sánchez-Sánchez, L. Vázquez, E. Blanco, M.D. Petit-Domínguez, J.Á. Martín-Gago, E. Casero, C. Quintana, Differential pulse voltammetric determination of the carcinogenic diamine 4,4′-oxydianiline by electrochemical preconcentration on a $MoS_2$ based sensor, Microchim. Acta 186 (2019) 793, https://doi.org/10.1007/s00604-019-3906-7.

[11] A.T.E. Vilian, B. Dinesh, S.M. Kang, U.M. Krishnan, Y.S. Huh, Y.K. Han, Recent advances in molybdenum disulfide-based electrode materials for electroanalytical applications, Microchim. Acta 186 (2019) 203, https://doi.org/10.1007/s00604-019-3287-y.

[12] S. Sharma, S. Singh, R.C. Singh, S. Sharma, Structural transformation and room temperature ammonia sensing properties of $TiS_2$ nanostructures, SN Appl. Sci. 2 (2020) 1–12, https://doi.org/10.1007/s42452-020-2647-x.

[13] B. Martín-García, D. Spirito, S. Bellani, M. Prato, V. Romano, A. Polovitsyn, R. Brescia, R. Oropesa-Nuñez, L. Najafi, A. Ansaldo, G. D'Angelo, V. Pellegrini, R. Krahne, I. Moreels, F. Bonaccroso, Extending the colloidal transition metal dichalcogenide library to $ReS_2$ nanosheets for application in gas sensing and electrocatalysis, Small 15 (2019), 1904670.

[14] N. Sakhuja, R.K. Jha, R. Chaurasiya, A. Dixit, N. Bhat, 1T-Phase titanium disulfide nanosheets for sensing $H_2S$ and $O_2$, ACS Appl. Nano Mater. 3 (2020) 3382–3394, https://doi.org/10.1021/acsanm.0c00127.

[15] Y. Xiong, H.W. Chen, D.W. Zhang, P. Zhou, Electronic and optoelectronic applications based on $ReS_2$, Phys. Status Solidi Rapid Res. Lett. 13 (2019) 1–14, https://doi.org/10.1002/pssr.201800658.

[16] N. Dhenadhayalan, M.I. Sriram, K.C. Lin, Aptamer-based fluorogenic sensing of interferon-gamma probed with $ReS_2$ and $TiS_2$ nanosheets, Sensor. Actuator. B Chem. 258 (2018) 929–936, https://doi.org/10.1016/j.snb.2017.11.178.

[17] Y. Huang, H. Deng, J. Zhang, H. Sun, W. Li, C. Li, Y. Zhang, D. Sun, A photoelectrochemical immunosensor based on $ReS_2$ nanosheets for determination of collagen III related to abdominal aortic aneurysm, Microchem. J. 168 (2021), 106363, https://doi.org/10.1016/j.microc.2021.106363.

[18] M.M. Fadhel, N. Ali, H. Rashid, N.M. Sapiee, A.E. Hamzah, M.S.D. Zan, N.A. Aziz, N. Arsad, A review on rhenium disulfide: synthesis approaches, optical properties, and applications in pulsed lasers, Nanomaterials 11 (2021), https://doi.org/10.3390/nano11092367.

[19] M. Carocho, M.F. Barreiro, P. Morales, I.C.F.R. Ferreira, Adding molecules to food , pros and cons : a review on synthetic and natural food additives, Compr. Rev. Food Sci. Food Saf. 13 (2014) 377–399, https://doi.org/10.1111/1541-4337.12065.

[20] F. Ivani de Andrade, M.I. Florindo Guedes, Í.G. Pinto Vieira, N.F. PereiraMendes, P. A. Salmito Rodrigues, C.S. Costa Maia, M.M. Marques Ávila, L. de Matos Ribeiro, Determination of synthetic food dyes in commercial soft drinks by TLC and ion-pair HPLC, Food Chem. 157 (2014) 193–198, https://doi.org/10.1016/j.foodchem.2014.01.100.

[21] P. Amchova, H. Kotolova, J. Ruda-kucerova, Health safety issues of synthetic food colorants, Regul. Toxicol. Pharmacol. 73 (2015) 914–922, https://doi.org/10.1016/j.yrtph.2015.09.026.

[22] A. Maria de Souza Santos Cheibub, E. Silva Bahiense de Lyra, B. Jardim Alves, R. Andrade Donagemma, A. Duarte Pereira Netto, Development and validation of a multipurpose and multicomponent method for the simultaneous determination of six synthetic dyes in different foodstuffs by HPLC-UV-DAD, Food Chem. 323 (2020), 126811, https://doi.org/10.1016/j.foodchem.2020.126811.

[23] H. Yang, G. Ran, J. Yan, H. Zhang, X. Hu, A sensitive fluorescence quenching method for the detection of tartrazine with acriflavine in soft drinks, Luminiscence 33 (2018) 349–355, https://doi.org/10.1002/bio.3420.

[24] A. Peña-gonzalez, O. García-beltrán, E. Nagles, Detection of Sunset Yellow by Adsorption Voltammetry at Glassy Carbon Electrode Modified with Chitosan 13 (2018) 5005–5015, https://doi.org/10.20964/2018.05.35.

[25] H. Xu, X. Yang, G. Li, C. Zhao, X. Liao, Green synthesis of fluorescent carbon dots for selective detection of tartrazine in food samples, J. Agric. Food Chem. 63 (2015) 6707–6714, https://doi.org/10.1021/acs.jafc.5b02319.

[26] J. Yi, L. Zeng, Q. Wu, L. Yang, T. Xie, Sensitive simultaneous determination of synthetic food colorants in preserved fruit samples by capillary electrophoresis with contactless conductivity detection, Food Anal. Methods 11 (2018) 1608–1618, https://doi.org/10.1007/s12161-017-1141-6.

[27] A.P. Nambiar, M. Sanyal, P.S. Shrivastav, Simultaneous densitometric determination of eight food colors and four sweeteners in candies, jellies, beverages and pharmaceuticals by normal-phase high performance thin-layer chromatography using a single elution protocol, J. Chromatogr., A 1572 (2018) 152–161, https://doi.org/10.1016/j.chroma.2018.08.059.

[28] S.C. Chaves, P.N.C. Aguiar, L.M.F.C. Torres, E.S. Gil, R.C.S. Luz, F.S. Damos, R.A. A. Munoz, E.M. Richter, W.T.P. dosSantos, Simultaneous determination of caffeine, ibuprofen, and paracetamol by flow-injection analysis with multiple-pulse amperometric detection on boron-doped diamond electrode, Electroanalysis 27 (2015) 2785–2791, https://doi.org/10.1002/elan.201500306.

[29] P.B. Deroco, R.A. Medeiros, R.C. Rocha-Filho, O. Fatibello-Filho, Selective and simultaneous determination of indigo carmine and allura red in candy samples at the nano-concentration range by flow injection analysis with multiple pulse amperometric detection, Food Chem. 247 (2018) 66–72, https://doi.org/10.1016/j.foodchem.2017.12.006.

[30] M.J. Cadena, R. Misiego, K.C. Smith, A. Avila, B. Pipes, R. Reifenberger, A. Raman, Sub-surface imaging of carbon nanotube-polymer composites using dynamic AFM methods, Nanotechnology 24 (2013), https://doi.org/10.1088/0957-4484/24/13/135706.

[31] M.D. Petit-Domínguez, C. Quintana, L. Vázquez, M. del Pozo, I. Cuadrado, A. M. Parra-Alfambra, E. Casero, Synergistic effect of $MoS_2$ and diamond nanoparticles in electrochemical sensors: determination of the anticonvulsant drug valproic acid, Microchim. Acta 185 (2018) 334, https://doi.org/10.1007/s00604-018-2793-7.

[32] A. Coloma, M. del Pozo, R. Martínez-Moro, E. Blanco, P. Atienzar, L. Sánchez, M. D. Petit-Domínguez, E. Casero, C. Quintana, $MoS_2$ quantum dots for on-line fluorescence determination of the food additive allura red, Food Chem. 345 (2021), 128628, https://doi.org/10.1016/j.foodchem.2020.128628.

[33] A. Krüger, F. Kataoka, M. Ozawa, T. Fujino, Y. Suzuki, A.E. Aleksenskii, A.Y. Vul', E. Osawa, Unusually tight aggregation in detonation nanodiamond: identification and disintegration, Carbon N. Y. 43 (2005) 1722–1730, https://doi.org/10.1016/j.carbon.2005.02.020.

[34] X.F. Qiao, J. Bin Wu, L. Zhou, J. Qiao, W. Shi, T. Chen, X. Zhang, J. Zhang, W. Ji, P. H. Tan, Polytypism and unexpected strong interlayer coupling in two-dimensional layered $ReS_2$, Nanoscale 8 (2016) 8324–8332, https://doi.org/10.1039/c6nr01569g.

[35] J.Y. Park, H.E. Joe, H.S. Yoon, S. Yoo, T. Kim, K. Kang, B.K. Min, S.C. Jun, Contact effect of $ReS_2$/metal interface, ACS Appl. Mater. Interfaces 9 (2017) 26325–26332, https://doi.org/10.1021/acsami.7b06432.

[36] L.W. Wong, L. Huang, F. Zheng, Q.H. Thi, J. Zhao, Q. Deng, T.H. Ly, Site-specific electrical contacts with the two-dimensional materials, Nat. Commun. 11 (2020) 1–10, https://doi.org/10.1038/s41467-020-17784-3.

[37] Z. Zhang, K. Yao, Y. Liu, C. Jin, X. Liang, Q. Chen, L.M. Peng, Quantitative analysis of current-voltage characteristics of semiconducting nanowires: decoupling of contact effects, Adv. Funct. Mater. 17 (2007) 2478–2489, https://doi.org/10.1002/adfm.200600475.

[38] J. Čermák, H. Kozak, Š. Stehlík, V. Švrček, V. Pichot, D. Spitzer, A. Kromka, B. Rezek, Microscopic electrical conductivity of nanodiamonds after thermal and plasma treatments, MRS Adv 1 (2016) 1105–1111, https://doi.org/10.1557/adv.2016.112.

[39] T. Kondo, I. Neitzel, V.N. Mochalin, J. Urai, M. Yuasa, Y. Gogotsi, Electrical conductivity of thermally hydrogenated nanodiamond powders, J. Appl. Phys. 113 (2013), 214307, https://doi.org/10.1063/1.4809549.

[40] A.A. Fokin, P.R. Schreiner, Band gap tuning in nanodiamonds: first principle computational studies, Mol. Phys. 107 (2009) 823–830, https://doi.org/10.1080/00268970802649625.

[41] P.A. Kolozof, A.B. Florou, K. Spyrou, J. Hrbac, M.I. Prodromidis, In-situ tailoring of the electrocatalytic properties of screen-printed graphite electrodes with sparked generated molybdenum nanoparticles for the simultaneous voltammetric determination of sunset yellow and tartrazine, Sensor. Actuator. B Chem. 304 (2020), 127268, https://doi.org/10.1016/j.snb.2019.127268.

[42] K. Marquez-Mariño, J. Penagos-Llanos, O. García-Beltrán, E. Nagles, J.J. Hurtado, Development of a novel electrochemical sensor based on a carbon paste electrode decorated with $Nd_2O_3$ for the simultaneous detection of tartrazine and sunset yellow, Electroanalysis 30 (2018) 2760–2767, https://doi.org/10.1002/elan.201800550.

[43] T. Wu, Q. Wang, X. Peng, Y. Guo, Facile synthesis of gold/graphene nanocomposites for simultaneous determination of sunset yellow and tartrazine in soft drinks, Electroanalysis (2021) 1–9, https://doi.org/10.1002/elan.202100464.

[44] T. Gan, J. Sun, W. Meng, L. Song, Y. Zhang, Electrochemical sensor based on graphene and mesoporous $TiO_2$ for the simultaneous determination of trace colourants in food, Food Chem. 141 (2013) 3731–3737, https://doi.org/10.1016/j.foodchem.2013.06.084.

[45] Y. Shen, X. Zhang, W. Prinyawiwatkul, Z. Xu, Simultaneous determination of red and yellow artificial food colourants and carotenoid pigments in food products, Food Chem. 157 (2014) 553–558, https://doi.org/10.1016/j.foodchem.2014.02.039.

[46] K. Deng, C. Li, X. Li, H. Huang, Simultaneous detection of sunset yellow and tartrazine using the nanohybrid of gold nanorods decorated graphene oxide, J. Electroanal. Chem. 780 (2016) 296–302, https://doi.org/10.1016/j.jelechem.2016.09.040.

[47] X. Ye, Y. Du, D. Lu, C. Wang, Fabrication of β-cyclodextrin-coated poly (diallyldimethylammonium chloride)-functionalized graphene composite film modified glassy carbon-rotating disk electrode and its application for simultaneous electrochemical determination colorants of sunset yello, Anal. Chim. Acta 779 (2013) 22–34, https://doi.org/10.1016/j.aca.2013.03.061.

[48] M.R. Majidi, R. Fadakar Bajeh Baj, A. Naseri, Carbon nanotube-ionic liquid (CNT-IL) nanocamposite modified sol-gel derived carbon-ceramic electrode for simultaneous determination of sunset yellow and tartrazine in food samples, Food Anal. Methods 6 (2013) 1388–1397, https://doi.org/10.1007/s12161-012-9556-6.

[49] R.A. Medeiros, B.C. Lourencao, R.C. Rocha-Filho, O. Fatibello-Filho, Flow injection simultaneous determination of synthetic colorants in food using multiple pulse amperometric detection with a boron-doped diamond electrode, Talanta 99 (2012) 883–889, https://doi.org/10.1016/j.talanta.2012.07.051.

[50] C. of the E. Union, European Parliament and Council Directive 94/35/EC of 30 June 1994 of sweeteners for use in foodstuffs (1994). Https://Op.Europa.Eu/En/Publication-Detail/-/Publication/576c6110-0270-429a-B445-8bdb40025cb4/Language-En.